




Isomeric excitation of ^{229}Th via scanning tunneling microscope

Xue Zhang , Tao Li, Xu Wang ,* and Hui Dong [†]

Graduate School of China Academy of Engineering Physics, Number 10 Xibeiwang East Road, Haidian District, Beijing 100193, China



(Received 10 October 2023; revised 14 July 2024; accepted 22 July 2024; published 13 August 2024)

The low energy of the isomeric state of the radionuclide thorium-229 (^{229}Th) makes it highly promising for applications in fundamental physics, precision metrology, and quantum technologies. The direct access to the isomer state from the ground state has attracted significant attention. Here, we propose a tabletop approach utilizing the scanning tunneling microscope technique to induce excitation of a single ^{229}Th nucleus. With achievable parameters, the isomeric excitation rate is advantageous over existing methods, allowing the excitation and control of ^{229}Th on the single-nucleus level. It offers the unique potential of exciting and detecting subsequent γ decay from a single nucleus, providing a new direction for future experimental investigation of the ^{229}Th isomeric state.

DOI: [10.1103/PhysRevC.110.024608](https://doi.org/10.1103/PhysRevC.110.024608)

I. INTRODUCTION

Thorium-229 (^{229}Th) recently garnered significant attention due to its low-lying isomeric state [1,2], which is only 8.3 eV above the nuclear ground state [3,4]. It is an appealing candidate for various applications in constructing nuclear optical clocks [5–8], detecting temporal variations of fundamental constants [9–11], measuring gravitational shifts [12,13], etc. The isomeric state can be obtained from nuclear decay reactions [4,14,15]. Nevertheless, to allow control and to facilitate the applications, extensive research efforts have been made to explore active nuclear-excitation approaches, using vacuum ultraviolet (VUV) light sources [16–20], high-energy synchrotron radiations [21,22], laser pulses [23–28], electrons [29,30], muons [31,32], etc. Currently, experimental demonstrations are reported with high-energy synchrotron radiations [22], laser-generated plasmas [24], and VUV sources [19,20].

In this paper, we propose a completely new experimental setup using the tabletop scanning tunneling microscope (STM) to excite the ^{229}Th atomic nucleus to its isomeric state ^{229m}Th . STM is a powerful imaging technique used in nanotechnology and surface science [33,34]. With the high spatial control of a metallic tip of the STM, a single ^{229}Th atom can be located and controlled, as illustrated in Fig. 1. The metal tip with radius of curvature R_t is positioned above a substrate plane with distance d . Both the tip and substrate are typically made of a noble metal, e.g., silver (Ag) [35,36]. After applying a bias voltage V_b , electrons will tunnel through the vacuum between the tip and the substrate and excite the ^{229}Th nucleus from the ground state to the isomeric state. Here, we mainly focus on the excitation of the ^{229}Th nucleus with the STM.

The current approach offers advantages of isomeric-excitation efficiency, precise manipulation, and photon-detection efficiency. First, a considerable excitation rate is achievable with STM method. In Table I, we show the comparison of the excitation rates among the current method, laser excitation, and the electron beam excitation. With tip radius $R_t = 0.5$ nm, tip-substrate distance $d = 0.2$ nm, and bias voltage $V_b = -11$ V, the isomeric excitation rate is on the order of 10^{-3} s^{-1} in our setup, contrasting with the excitation rates on the order of 10^0 s^{-1} achieved with laser pulse and electron beam excitation. The detailed comparison process is shown in Appendix A. Second, the STM allows the precise focus of electronic current on the level pA to an area of nm scale [37], and excitation and control of a located single ^{229}Th nucleus. And the experimental technique of the STM also allows multiple tips [38,39], which can increase the excitation rate by one to two orders of magnitude. Finally, the current tabletop setup enables the application of the experimental technique of highly efficient luminescence detection with the detection solid angle about 3 sr [40,41], which is much greater than the solid angle of about 0.1 sr in the synchrotron radiation excitation experiment [22]. Efficient photon collection allows the detection of the weak photon signals from the radiative decay of ^{229m}Th , and further increases the effective excitation rate. These advantages make the current method highly promising for achieving excitation, control, and detection of ^{229}Th especially on the single-nucleus level, which is not achievable with other methods.

II. THEORY OF ISOMERIC EXCITATION USING THE STM

In this part we develop a quantum theory of isomeric excitation particularly for the STM setup. The total Hamiltonian of the system is $H = H_{\text{el}} + H_n + H_{\text{int}}$, where $H_{\text{el}}(H_n)$ represents the Hamiltonian of the tunneling electron (the ^{229}Th nucleus) and H_{int} is the interaction between them. The Hamiltonian of the tunneling electron is $H_{\text{el}} = -\nabla^2/2m_e + V(\mathbf{r})$, where $V(\mathbf{r})$

*Contact author: xwang@gscaep.ac.cn

[†]Contact author: hdong@gscaep.ac.cn

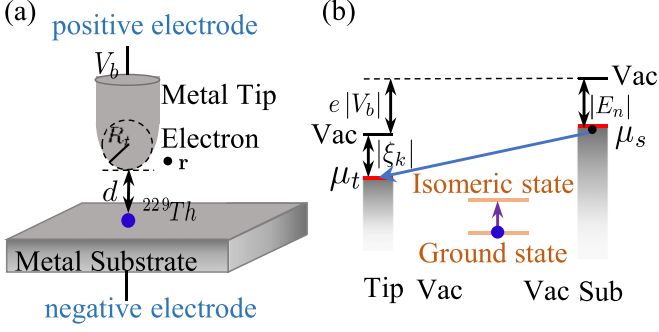


FIG. 1. Schematic illustration of STM with a single ^{229}Th atom on a substrate. The STM tip apex is modeled as a sphere with radius R_t . The position of the ^{229}Th atom (blue dot), just below the center of the tip, is set as the origin of the coordinate system, and d is the distance between the tip and substrate. \mathbf{r} stands for the position of the tunneling electron (black dot), and V_b is the bias voltage applied to the tip and substrate. (b) The energy level diagram at negative bias voltage. The black lines denote the vacuum level for two electrodes, and the red lines represent the initial and final electronic states. $\mu_t \equiv \mu_0 + eV_b$ and $\mu_s \equiv \mu_0$ are the Fermi energies of the tip and the substrate at the bias voltage V_b , where μ_0 is the Fermi energy of the tip and the substrate at zero bias.

is the potential felt by the tunneling electron at the position \mathbf{r} [43,44]. The wave functions are found for different regions as [43–46]

$$\begin{aligned} H_{\text{el},t}|\phi_k\rangle &\simeq \tilde{\xi}_k|\phi_k\rangle, \\ H_{\text{el},s}|\varphi_n\rangle &\simeq \tilde{E}_n|\varphi_n\rangle, \end{aligned} \quad (1)$$

where $H_{\text{el},t}$ ($H_{\text{el},s}$) is the Hamiltonian of the free tip (substrate) obtained by neglecting the potential in the substrate (tip) region. $|\phi_k\rangle$ ($|\varphi_n\rangle$) is the eigenstate of the free tip (substrate) with $\tilde{\xi}_k \equiv \xi_k + eV_b$ ($\tilde{E}_n \equiv E_n$), where ξ_k (E_n) is the eigenenergy with zero bias voltage. Here we neglect the change of the wave function of the tip induced by the applied voltage [47]. The detailed forms of these wave functions are presented in Appendix B.

The Hamiltonian of the ^{229}Th atomic nucleus is simplified as a two-level system $H_n = \epsilon_g|g\rangle\langle g| + \epsilon_e|e\rangle\langle e|$, where $|g\rangle$ ($|e\rangle$) is its ground (isomeric excited) state with energy ϵ_g (ϵ_e). We assume that the energy gap is $\Delta_{\text{eg}} \equiv \epsilon_e - \epsilon_g = 8.338$ eV [4].

TABLE I. Comparison of single-nucleon excitation probabilities found in the literature and their calculated total excitation rates. We use the density of the Th nuclei 10^{18} cm^{-3} , the area 1 mm^2 , and the target thickness 10 nm to estimate total transition rate of other methods. In the electron beam excitation, we use the cross section 10^{-25} cm^2 under the current 100 μA . And in the laser excitation, the repetition rate of the laser is 10 Hz.

Method	Excitation probability (s^{-1} per nucleus)	Total transition rate (s^{-1})
Our paper	10^{-3}	10^{-3}
Electron beam [29,30]	10^{-10}	10^1
Laser [27,42]	10^{-11} per pulse	10^1

The interaction between the electron and nucleus is given by [48]

$$H_{\text{int}} = -\frac{1}{c} \int \mathbf{J}(\mathbf{R}) \cdot \mathbf{A}(\mathbf{R}) d\mathbf{R}, \quad (2)$$

where $\mathbf{J}(\mathbf{R})$ is the nucleus current operator at position \mathbf{R} . $\mathbf{A}(\mathbf{R})$ is the electromagnetic vector potential generated by the tunneling electron with current $\mathbf{j}(\mathbf{r})$:

$$\mathbf{A}(\mathbf{R}) = \frac{1}{c} \int \frac{e^{ik|\mathbf{r}-\mathbf{R}|}}{|\mathbf{r}-\mathbf{R}|} \cdot \mathbf{j}(\mathbf{r}) d\mathbf{r}, \quad (3)$$

where $k\hbar c = (\tilde{E}_n - \tilde{\xi}_k)$ corresponds to the energy loss of the electron. The electron current is obtained as $\mathbf{j}_{fi}(\mathbf{r}) = -e\hbar(\psi_f \nabla \psi_i^* - \psi_i^* \nabla \psi_f)/2m_e$ [34,45]. And ψ_i (ψ_f) denotes the wave function of the initial (final) state of the electron. For negative bias $V_b < 0$, the electron flies from the substrate to the tip, i.e., $\psi_i = \varphi_n(\mathbf{r})$ and $\psi_f = \phi_k(\mathbf{r})$.

From Fermi's golden rule, the transition probability per unit time from an initial state $|i\rangle$ to a final state $|f\rangle$ is written as

$$P_{fi} = \frac{2\pi}{\hbar} |\langle f|H_{\text{int}}|i\rangle|^2 \delta(\mathcal{E}_i - \mathcal{E}_f), \quad (4)$$

where for the current system $|i\rangle \equiv |J_i M_i\rangle \otimes |\varphi_n\rangle$ and $|f\rangle \equiv |J_f M_f\rangle \otimes |\phi_k\rangle$ are the product states of the nucleus and the electron. Here J_i (J_f) and M_i (M_f) are the angular momentum and magnetic quantum numbers of the nuclear ground (isomeric) state, respectively. The initial and final energies are $\mathcal{E}_i = \epsilon_g + \tilde{E}_n$ and $\mathcal{E}_f = \epsilon_e + \tilde{\xi}_k$.

Here we use multipole expansion [48]:

$$\frac{e^{ik|\mathbf{r}-\mathbf{R}|}}{|\mathbf{r}-\mathbf{R}|} = 4\pi ik \sum_{T,l,m} \mathcal{A}_{lm}^T(kR) \mathcal{B}_{lm}^T(kr). \quad (5)$$

The transition type \mathcal{T} can be either E (electric) or M (magnetic). And $\mathcal{A}_{lm}^T(kR)$ is the multipole vector potential, $\mathcal{A}_{lm}^M(kR) = 1/\sqrt{l(l+1)} \mathbf{L} j_l(kR) Y_{lm}(\hat{\mathbf{R}})$ and $\mathcal{A}_{lm}^E(kR) = -i/(k\sqrt{l(l+1)}) \nabla \times \mathbf{L} j_l(kR) Y_{lm}(\hat{\mathbf{R}})$. Here $Y_{lm}(\hat{\mathbf{R}})$ are spherical harmonics. The potential $\mathcal{B}_{lm}^T(kr)$ can be obtained from $\mathcal{A}_{lm}^T(kR)$ by replacing the Bessel function $j_l(kR)$ with the Hankel function of the first kind $h_l^{(1)}(kr)$. Then the transition matrix element $\langle f|H_{\text{int}}|i\rangle$ turns into [29,30,48]

$$\begin{aligned} \langle f|H_{\text{int}}|i\rangle &= \sum_{\mathcal{T}} \langle f|H_{\text{int}}^{\mathcal{T}}|i\rangle \\ &= -\frac{4\pi ik}{c^2} \sum_{T,l,m} \int \mathbf{J}_{fi}(\mathbf{R}) \cdot \mathcal{A}_{lm}^T(kR) d\mathbf{R} \\ &\quad \times \int \mathbf{j}_{fi}(\mathbf{r}) \cdot \mathcal{B}_{lm}^T(kr) d\mathbf{r}. \end{aligned} \quad (6)$$

The first integral in the above equation associated to the nuclear transition current $\mathbf{J}_{fi}(\mathbf{R})$ is derived with the form [29]

$$\begin{aligned} \int \mathbf{J}_{fi}(\mathbf{R}) \cdot \mathcal{A}_{lm}^T(kR) d\mathbf{R} &= \frac{ik^l c}{(2l+1)!!} \sqrt{\frac{l+1}{l}} \\ &\quad \times |\langle J_f M_f | \mathcal{M}_{lm}^T | J_i M_i \rangle|, \end{aligned} \quad (7)$$

where the nuclear transition matrix element is related to the reduced probability $B(Tl; J_i \rightarrow J_f)$ of nuclear transition [29]:

$$B(Tl; J_i \rightarrow J_f) = \frac{1}{2J_i + 1} \sum_{M_i, M_f, m} |\langle J_f M_f | \mathcal{M}_{lm}^T | J_i M_i \rangle|^2. \quad (8)$$

The second integral of Eq. (6), $\Xi_{fi}^{Tl} \equiv \int \mathbf{j}_{fi}(\mathbf{r}) \cdot \mathcal{B}_{lm}^T(kr) d\mathbf{r}$, is associated to the electronic transition and can be deduced into the following forms:

$$\Xi_{fi}^{El} \approx -\frac{eicl}{\sqrt{l(l+1)}} \int \phi_k(\mathbf{r}) \varphi_n(\mathbf{r}) h_l^{(1)}(kr) Y_{lm}(\hat{\mathbf{r}}) d\mathbf{r}, \quad (9)$$

$$\Xi_{fi}^{Ml} = 0, \quad (10)$$

where Ξ_{fi}^{El} is given to the leading order according to the condition $kr \ll 1$. Detailed derivations and discussions on Ξ_{fi}^{Tl} are presented in Appendix C.

The overall transition probability per unit time is obtained explicitly as

$$P = \sum_{l,m} \frac{2\pi}{\hbar} \left(\frac{4\pi k}{c} \right)^2 \frac{k^{2l}}{[(2l+1)!!]^2} \frac{B(El; J_i \rightarrow J_f) \delta(\mathcal{E}_i - \mathcal{E}_f)}{\int dE_n \rho_s(E_n)} \times \frac{l+1}{l(2l+1)} \sum_{n,k} F_{\mu_0, T}(E_n) [1 - F_{\mu_0, T}(\xi_k)] |\Xi_{fi}^{El}|^2, \quad (11)$$

where $\rho_s(E)$ [$\rho_t(E)$] is the density of state at the substrate (tip). $F_{\mu_0, T}(E)$ is the Fermi-Dirac distribution of electrons in tip or substrate state with chemical potential μ_0 and temperature T . In an STM experiment, the temperature of the ultrahigh-vacuum chamber is low enough, typically lower than 10 K [49,50], that the Fermi-Dirac distribution function is approximately a Heaviside function, i.e., $F_{\mu_0, T}(E) = 1$ for $E < \mu_0$ and $F_{\mu_0, T}(E) = 0$ for $E > \mu_0$. The transition probability per unit time is simplified as

$$P = \sum_{l,m} \frac{2\pi}{\hbar} \left(\frac{4\pi k}{c} \right)^2 \frac{k^{2l}}{[(2l+1)!!]^2} \frac{l+1}{l(2l+1)} \frac{B(El; J_i \rightarrow J_f)}{\int dE_n \rho_s(E_n)} \times \int_{\mu_0 + \Delta_{\text{eg}} + eV_b}^{\mu_0} dE_n \rho_s(E_n) \rho_t(\xi_k) |\Xi_{fi}^{El}|^2, \quad (12)$$

where $\xi_k = E_n - \Delta_{\text{eg}} - eV_b$.

Without loss of generality, we consider the material of the tip and the substrate to be Ag, the density of states of which is obtained from Ref. [51] (see Appendix D for details). In the calculation, we use the reduced nuclear transition probability $B(E2; J_f \rightarrow J_i) = 27.04$ Weisskopf units [52].

III. NUMERICAL RESULTS

Figure 2(a) shows the transition probability P per unit time as a function of the tip radius R_t , for fixed tip position $d = 0.5$ nm and applied bias voltage $V_b = -11$ V. The curve shows an exponential decay with the increase of the tip radius. In Eq. (12), the tip radius R_t affects the transition probability via the interaction strength Ξ_{fi}^{El} . A larger needle tip radius leads to a weaker electric field strength at the tip, yielding a lower isomeric excitation probability. And a smaller tip radius leads to a higher isomeric transition probability.

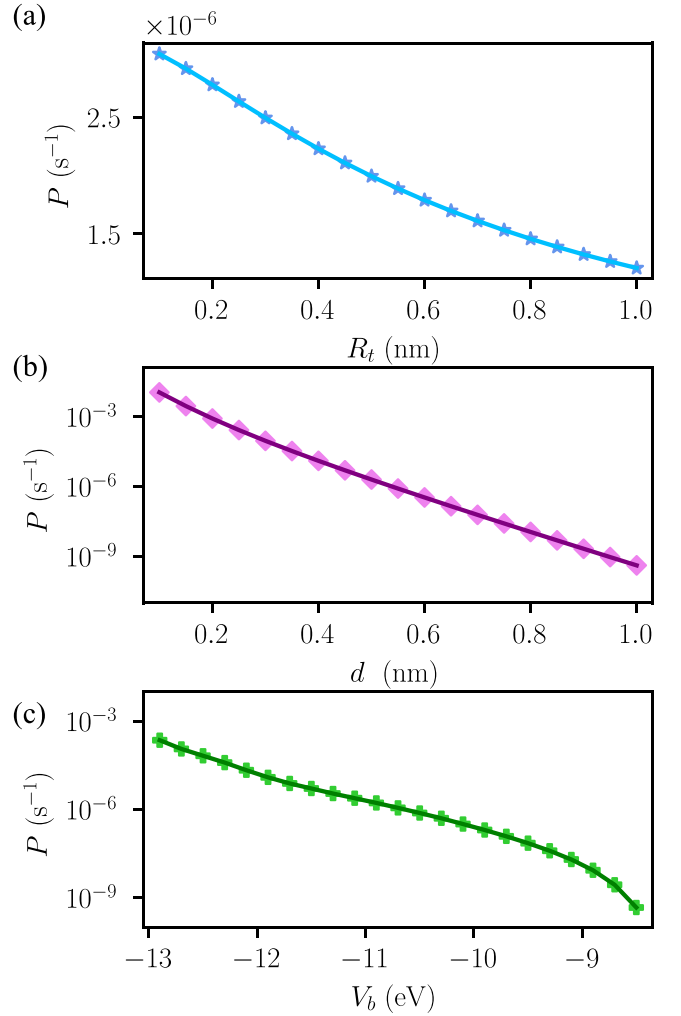


FIG. 2. Transition probability per unit time P as a function of tip radius R_t , distance from the tip to the substrate d , and applied bias voltage V_b . (a) Dependency of P on R_t , with d fixed at 0.5 nm and V_b set to -11 V. (b) Dependency of P on d , with R_t fixed at 0.5 nm and V_b set to -11 V. (c) Dependency of P on V_b , with R_t fixed at 0.5 nm and d fixed at 0.5 nm. Symbols are numerical results, and curves are added to guide the eye.

Figure 2(b) presents the dependency of the transition probability P on the tip-substrate distance d , with R_t fixed at 0.5 nm and V_b set to -11 V. The data show that the transition probability P decreases exponentially with the increase of d . This is attributed to the decreasing overlap of wave functions between the tip and the substrate as the distance increases. A larger wave-function overlap facilitates electron tunneling between the tip and substrate, leading to an enhanced isomeric excitation probability.

Figure 2(c) shows an approximately exponential dependency of the transition probability P on the applied bias voltage V_b , in which both d and R_t are fixed at 0.5 nm. In Eq. (12), the bias voltage V_b mainly determines the range of the energy integration. A higher V_b expands the integration range, thus allowing a broader range of energy levels to contribute to the isomeric excitation.

We also considered the impact of positive bias voltage and small displacements of the tip position relative to the atomic center on the transition probability. Detailed calculations and results are provided in Appendixes E and F, respectively.

IV. DISCUSSIONS

For a typical STM setup with tip radius $R_t = 0.5$ nm, tip-substrate distance $d = 0.2$ nm, and bias voltage $V_b = -11$ V, the isomeric excitation rate is on the order of 10^{-3} s $^{-1}$ per nucleus. Typically, the ^{229}Th atoms are assumed to be doped in a wide-band-gap crystal, such as CaF_2 , to suppress the internal conversion process [21,53,54]. We would like to remark that the use of crystals will induce parasitic signals, such as Cherenkov photon radiation (<200 nm) with energies larger than 158 keV [55] and luminescence of CaF_2 (>200 nm) by creating electron-hole pairs which form self-trapped excitons [56]. These parasitic signals post a challenge to detect the photon signal produced by the gamma decay of the ^{229m}Th . Yet, experiments [4,19,20] have shown signs of successful identification of the signal from parasitic signals.

Here the voltage selection is within the bandwidth of a large-band-gap crystal to prevent damage to the crystal [54]. In traditional STM, the tunneling current is 10^{-1} pA at a bias voltage of 2 V and tip-substrate distance of 0.8 nm [57]. For every 0.1 nm closer to the substrate, the current increases by one order of magnitude. With 0.2-nm tip-substrate distance, the current is on the order of μA (10^{12} electrons per second). This electron beam would not induce a change in the crystal structure.

The excitation rate can be further enhanced for the current STM method. First, wider band-gap crystals allow higher applied bias voltages and hence higher excitation rates. Second, smaller tip-substrate distances (without burning out the crystal) and the excitation with multiple tips allow higher excitation rate. For example, the excitation rate of 10^0 s $^{-1}$ is achieved with the tip radius $R_t = 0.3$ nm, tip-substrate distance $d = 0.1$ nm, bias voltage $V_b = -13$ V, and the tips number of 10. Together with the high photon collection efficiency of the STM, the current method with the STM has considerable advantage to investigate the ^{229}Th isomer state.

We would like to remark that the experimental detection of exciting ^{229}Th nuclei via the STM depends not only on the excitation probability, but also on the deexcitation process of ^{229m}Th . In addition to emitting photons through gamma decay, ^{229m}Th may also release energy through inelastic scattering with conduction electrons in the metal substrate without emitting photons [29]. The actual proportion of different deexcitation processes in the decay of ^{229m}Th in our system needs further investigation to ensure the observation of the excitations.

V. CONCLUSION

In summary, we have proposed a new approach to use tunneling electrons in an STM to excite the thorium-229 nucleus from the ground state to the low-lying isomeric state. The tunneling electrons, under an applied bias voltage, pass through the vacuum between the tip and the substrate and

excite the ^{229}Th nucleus. A comprehensive theoretical framework is developed to calculate the isomeric excitation rate, and to investigate the dependency of the excitation rate on key STM parameters, including the tip radius, the tip-substrate distance, and the applied bias voltage. The calculated single-nucleus excitation rate is advantageous over existing methods. More importantly, our method allows nuclear excitation and control on the single-nucleus level, which is unique among all existing methods and proposals. The possibility of exciting, controlling, and detecting nuclear radiative decay on the single-nucleus level points to a completely new territory of studying nuclear physics as well as quantum optics.

ACKNOWLEDGMENTS

This work is supported by the Innovation Program for Quantum Science and Technology (Grant No. 2023ZD0300700) and the National Natural Science Foundation of China (Grants No. U2230203, No. U2330401, and No. 12088101).

APPENDIX A: COMPARISON BETWEEN THE CURRENT STM METHOD AND PREVIOUS APPROACHES

Here, we show the detailed comparison of the excitation rate among the current method, laser excitation, and electron beam excitation.

1. Current method with STM

With tip radius $R_t = 0.5$ nm, tip-substrate distance $d = 0.2$ nm, and bias voltage $V_b = -11$ V, the isomeric excitation rate of our STM method is 10^{-3} s $^{-1}$.

2. Electron beam excitation

We consider low-energy electron beam (≈ 10 eV) excitation [29,30] with cross section $\sigma = 10^{-25}$ cm 2 . With the density of the nuclei $\rho_N = 10^{18}$ cm $^{-3}$, the target thickness $D = 10$ nm, and the current [58] $I = 100$ μA , the isomeric excitation rate $\sigma\rho_N DI/e$ is 10^1 s $^{-1}$.

3. Laser excitation

We consider direct laser excitation [27,42] with the transition probability $r_L = 10^{-10}$ s $^{-1}$ per nuclei after a laser pulse with 5-ns duration. With the density of the nuclei $\rho_N = 10^{18}$ cm $^{-3}$, the laser light focused area $S = 1$ mm 2 , the target thickness $D = 10$ nm, and $f = 10$ Hz repetition rate, the isomeric excitation rate $r_L\rho_N SDf$ is 10^1 s $^{-1}$.

These excitation rates are listed in Table I in the main text.

APPENDIX B: ELECTRON WAVE FUNCTIONS

In the current discussion, the tip apex is considered as a metallic sphere with its wave function in the vacuum region as an asymptotic spherical shape:

$$\phi_k(\mathbf{r}) = A_k \frac{\exp[-\kappa_k(|\mathbf{r} - \mathbf{a}| - R_t)]}{\kappa_k |\mathbf{r} - \mathbf{a}|}, \quad (\text{B1})$$

where $\mathbf{a} = (0, 0, d + R_t)$ is the position of the center of the tip and R_t is the radius of curvature of the tip. $\kappa_k = \sqrt{-2m_e \xi_k}/\hbar$ is the attenuation factor and A_k is the normalization coefficient. We choose the area below the needle tip as the integration area in the later calculation. Assuming the center of the tip is the origin, i.e., $\mathbf{a} = 0$, we get normalization coefficient $A_k = \sqrt{\kappa_k^3/\pi}$ according to normalization conditions $\int d\mathbf{r} |\phi_k(\mathbf{r})|^2 = 1$. This wave function is typical known as the s wave, which is the simplest case for the tip [47]. The surface wave function of the bare metal substrate in the vacuum region takes the form [34,59]

$$\varphi_n(\mathbf{r}) = B_n \exp(-\kappa_n |z|), \quad (\text{B2})$$

where $\kappa_n = \sqrt{-2m_e E_n}$ is the attenuation factor and B_n is the normalization coefficient. Since the wave function of metal surface waves only exists in the upper half plane (i.e., $z > 0$), we obtain $B_n = \sqrt{2\kappa_n}$ according to normalization conditions $\int d\mathbf{r} |\varphi_n(\mathbf{r})|^2 = 1$. Experiments have shown that the insulating layer on the metal surface does not change the line shape of the substrate-photon-emission spectrum but only reduces its intensity [60].

APPENDIX C: ELECTRON TRANSITION MATRIX ELEMENT Ξ_{fi}^{Tl}

We get the current $\mathbf{j}_{fi}(\mathbf{r})$ of the electron tunneling from the substrate to the tip as

$$\mathbf{j}_{fi}(\mathbf{r}) = -e \frac{i\hbar}{2m_e} (\phi_k \nabla \varphi_n - \varphi_n \nabla \phi_k). \quad (\text{C1})$$

With the expression of $\mathcal{B}_{lm}^E(kr)$ in the main paper, we calculate electron transition matrix element Ξ_{fi}^{Tl} :

$$\Xi_{fi}^{El} = \frac{-i}{k\sqrt{l(l+1)}} \int d\mathbf{r} \mathbf{j}_{fi}(\mathbf{r}) \cdot \nabla \times \mathbf{L} h_l^{(1)}(kr) Y_{lm}(\hat{\mathbf{r}}), \quad (\text{C2})$$

$$\Xi_{fi}^{Ml} = \frac{1}{\sqrt{l(l+1)}} \int d\mathbf{r} \mathbf{j}_{fi}(\mathbf{r}) \cdot \mathbf{L} h_l^{(1)}(kr) Y_{lm}(\hat{\mathbf{r}}), \quad (\text{C3})$$

where $k\hbar c = \tilde{E}_n - \tilde{\xi}_k$ is the energy lost by tunneling electrons, corresponding to the energy gap Δ_{eg} between the ground state and the excited state of the nucleus. With the identity $\nabla \times \mathbf{L} f_l(kr) Y_{lm}(\hat{\mathbf{r}}) = i \nabla \left\{ \frac{\partial}{\partial r} [r f_l(kr)] Y_{lm} \right\} + ik^2 \mathbf{r} f_l(kr) Y_{lm}(\hat{\mathbf{r}})$ and the flow conservation equation $\nabla \cdot \mathbf{j}_{fi} = ikc e \phi_k \varphi_n$, we get

$$\begin{aligned} \Xi_{fi}^{El} &= \frac{ic}{\sqrt{l(l+1)}} \int d\mathbf{r} \rho_{fi} \frac{\partial}{\partial r} [r h_l^{(1)}(kr)] Y_{lm}(\hat{\mathbf{r}}) \\ &+ \frac{k}{\sqrt{l(l+1)}} \int d\mathbf{r} \mathbf{j}_{fi}(\mathbf{r}) \cdot \mathbf{r} h_l^{(1)}(kr) Y_{lm}(\hat{\mathbf{r}}), \end{aligned} \quad (\text{C4})$$

where $\rho_{fi} = e \phi_k \varphi_n$ is a densitylike function.

Using the spherical coordinate system for simplicity of expression, we obtain

$$\begin{aligned} \Xi_{fi}^{El} &= -\frac{icl}{\sqrt{l(l+1)}} \int d\mathbf{r} \phi_k \varphi_n h_l^{(1)}(kr) Y_{lm}(\hat{\mathbf{r}}) \\ &+ \frac{ick}{\sqrt{l(l+1)}} \int d\mathbf{r} r \phi_k \varphi_n h_{l-1}^{(1)}(kr) Y_{lm}(\hat{\mathbf{r}}) \\ &+ \frac{i\hbar}{2m_e \sqrt{l(l+1)}} \int d\mathbf{r} \kappa_n r \cos \theta \phi_k \varphi_n h_l^{(1)}(kr) Y_{lm}(\hat{\mathbf{r}}) \end{aligned}$$

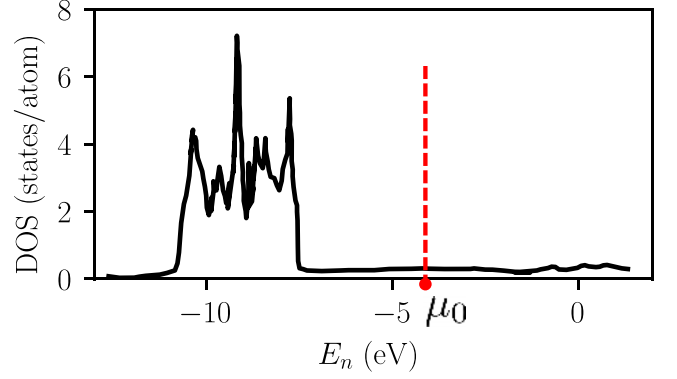


FIG. 3. The density of states (DOS) of Ag. $\mu_0 = -4.64$ eV is the fermi energy of Ag.

$$\begin{aligned} & -\frac{i\hbar}{2m_e} \frac{k}{\sqrt{l(l+1)}} \int d\mathbf{r} r^2 \phi_k \varphi_n h_l^{(1)}(kr) Y_{lm}(\hat{\mathbf{r}}) \\ & \times \frac{1 + \kappa_k |\mathbf{r} - \mathbf{a}|}{|\mathbf{r} - \mathbf{a}|^2} \\ & + \frac{i\hbar}{2m_e} \frac{k}{\sqrt{l(l+1)}} \int d\mathbf{r} k r \cos \theta \phi_k \varphi_n h_l^{(1)}(kr) Y_{lm}(\hat{\mathbf{r}}) \\ & \times \frac{1 + \kappa_k |\mathbf{r} - \mathbf{a}|}{|\mathbf{r} - \mathbf{a}|^2} \end{aligned} \quad (\text{C5})$$

and

$$\begin{aligned} \Xi_{fi}^{Ml} &= \frac{e\kappa_n}{\sqrt{l(l+1)}} \frac{\hbar^2}{2m_e} \int d\mathbf{r} \phi_k \varphi_n \\ & \times \left[\kappa_n + (R_t + d) \frac{1 + \kappa_k |\mathbf{r} - \mathbf{a}|}{|\mathbf{r} - \mathbf{a}|^2} \right] h_l^{(1)}(kr) \frac{\partial}{\partial \phi} Y_{lm}(\hat{\mathbf{r}}). \end{aligned} \quad (\text{C6})$$

In our setup, the wave functions $\phi_k(\mathbf{r})$ and $\varphi_n(\mathbf{r})$ have no component of angle ϕ , resulting in the vanishing component $\Xi_{fi}^{Ml} \propto \int d\phi \partial Y_{lm}(\hat{\mathbf{r}})/\partial \phi = 0$, due to $\partial Y_{lm}(\hat{\mathbf{r}})/\partial \phi \propto -ime^{-im\phi}$.

APPENDIX D: NUMERAL CALCULATIONS OF TRANSITION PROBABILITY

In this paper, we consider both the tip and substrate with the material of the silver (Ag). The density of states of Ag is presented in Fig. 3, obtained from Ref. [51]. In the numerical calculation, we select a cylinder with the height d as the integration area in a cylindrical coordinate system (r, ϕ, z) and ensure that the integral converges when the radius of the cylinder is reached. For the integration of energy E_n , we choose the number of energy intervals as 50 to ensure its convergence, and finally get the transition probability P in Fig. 2.

Figure 4 shows the transition probability as a function of tip radius R_t with different applied bias voltage V_b . For small bias voltages, nonmonotonic curves differing from those in the main text emerge. This is attributed to the increasing overlap of wave functions between the tip and substrate as the tip radius R_t decreasing at a small bias voltage. The larger overlap

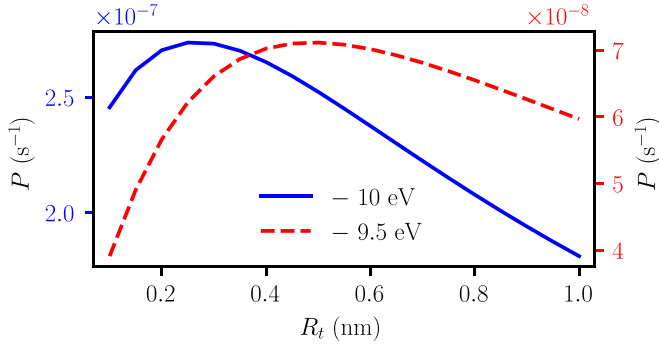


FIG. 4. Transition probability P as a function of tip radius R_t . The distance d is fixed at 0.5 nm and the applied bias voltage V_b is set to -10 V for blue solid line and -9.5 V for red dashed line, respectively.

facilitates electron tunneling between the tip and substrate, leading to an enhanced transition probability.

APPENDIX E: APPLIED POSITIVE BIAS VOLTAGE

We sketched the design of a single Th atom STM in Fig. 5 with applied positive bias voltage V_b . For positive bias, i.e., $V_b > 0$, the electron runs from the tip to the substrate [see Fig. 5(b)]. The electron tunneling current is

$$\mathbf{j}_{fi}^+(\mathbf{r}) = e \frac{i\hbar}{2m_e} (\phi_k \nabla \varphi_n - \varphi_n \nabla \phi_k), \quad (\text{E1})$$

which is the inverse of that in negative bias, i.e., $\mathbf{j}_{fi}^+(\mathbf{r}) = -\mathbf{j}_{fi}(\mathbf{r})$. This causes a slight change in Ξ_{fi}^{El} in Eq. (C5), but does not change its leading term. In conclusion, a variation in the applied bias electrode does not result in alteration of the transition probability P .

APPENDIX F: IMPACT OF THE POSITION OF THE TIP

One of the advantages in the current scheme is the precise location of the tip to allow the focus of the tunneling electrons on one single ^{229}Th . Here we consider the impact of the tip position with a small displacement relative to the center of the atom in the case of negative bias voltage. We assume the position of the center of the tip

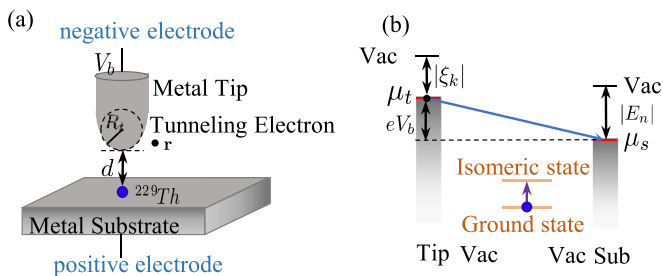


FIG. 5. Schematic diagram of STM of a single ^{229}Th with applied positive bias voltage V_b . (b) The level diagram for the inelastic electron scattering mechanism at bias voltage in (a). The symbols are the same as those in the main paper.

$\mathbf{a} = (a_x, a_y, d + R_t)$. Using the same calculation method, we can get

$$\begin{aligned} \Xi_{fi}^{El} = & -\frac{eicl}{\sqrt{l(l+1)}} \int d\mathbf{r} \phi_k \varphi_n h_l^{(1)}(kr) Y_{lm}(\hat{\mathbf{r}}) \\ & + \frac{eick}{\sqrt{l(l+1)}} \int d\mathbf{r} \phi_k \varphi_n r h_{l-1}^{(1)}(kr) Y_{lm}(\hat{\mathbf{r}}) \\ & + \frac{ei\hbar}{2m_e} \frac{k}{\sqrt{l(l+1)}} \kappa_n \int d\mathbf{r} \mathbf{r} \cos \theta \phi_k \varphi_n h_l^{(1)}(kr) Y_{lm}(\hat{\mathbf{r}}) \\ & - \frac{ei\hbar}{2m_e} \frac{k}{\sqrt{l(l+1)}} \int d\mathbf{r} [r^2 - r \cos \theta (R_t + d)] \\ & \times \phi_k \varphi_n h_l^{(1)}(kr) Y_{lm}(\hat{\mathbf{r}}) \frac{1 + \kappa_k |\mathbf{r} - \mathbf{a}|}{|\mathbf{r} - \mathbf{a}|^2} \\ & + \frac{ei\hbar}{2m_e} \frac{k}{\sqrt{l(l+1)}} \int d\mathbf{r} [r \sin \theta \cos \phi a_x \\ & + r \sin \theta \sin \phi a_y] \phi_k \varphi_n h_l^{(1)}(kr) Y_{lm}(\hat{\mathbf{r}}) \frac{1 + \kappa_k |\mathbf{r} - \mathbf{a}|}{|\mathbf{r} - \mathbf{a}|^2}. \end{aligned} \quad (\text{F1})$$

Since $kr \ll 1$, the first term is the leading term.

The electron matrix element Ξ_{fi}^{MI} is nonzero in this case because the tip wave function depends on the angle ϕ . We give the final expression of Ξ_{fi}^{MI} :

$$\begin{aligned} \Xi_{fi}^{MI} = & \frac{e\kappa_n}{\sqrt{l(l+1)}} \frac{\hbar^2}{2m_e} \int d\mathbf{r} \phi_k \varphi_n h_l^{(1)}(kr) \frac{\partial}{\partial \phi} Y_{lm}(\hat{\mathbf{r}}) \\ & + \frac{e}{\sqrt{l(l+1)}} \frac{\hbar^2}{2m_e} \int d\mathbf{r} \phi_k \varphi_n (R_t + d) \frac{1 + \kappa_k |\mathbf{r} - \mathbf{a}|}{|\mathbf{r} - \mathbf{a}|^2} \\ & \times h_l^{(1)}(kr) \frac{\partial}{\partial \phi} Y_{lm}(\hat{\mathbf{r}}) \\ & - \frac{e}{\sqrt{l(l+1)}} \frac{\hbar^2}{2m_e} \int d\mathbf{r} \phi_k \varphi_n a_x \frac{1 + \kappa_k |\mathbf{r} - \mathbf{a}|}{|\mathbf{r} - \mathbf{a}|^2} h_l^{(1)}(kr) \\ & \times \left(\sin \phi \frac{\partial}{\partial \theta} Y_{lm}(\hat{\mathbf{r}}) + \frac{\cos \theta}{\sin \theta} \cos \phi \frac{\partial}{\partial \phi} Y_{lm}(\hat{\mathbf{r}}) \right) \end{aligned}$$

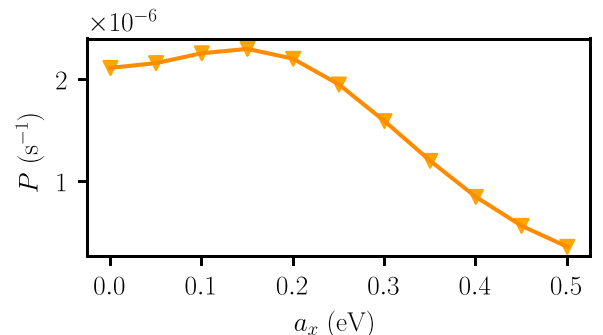


FIG. 6. Transition probability when the tip center is displaced relative to the center of the atom.

$$\begin{aligned}
& - \frac{e}{\sqrt{l(l+1)}} \frac{\hbar^2}{2m_e} \int d\mathbf{r} \phi_k \phi_n a_y \frac{1 + \kappa_k |\mathbf{r} - \mathbf{a}|}{|\mathbf{r} - \mathbf{a}|^2} h_l^{(1)}(kr) \\
& \times \left(-\cos\phi \frac{\partial}{\partial\theta} Y_{lm}(\hat{\mathbf{r}}) + \frac{\cos\theta}{\sin\theta} \sin\phi \frac{\partial}{\partial\phi} Y_{lm}(\hat{\mathbf{r}}) \right).
\end{aligned} \tag{F2}$$

The transition probability as a function of displacement is presented in Fig. 6. Here we assume $a_x = a_y$ for simplicity

and set the parameters to $d = 0.5$ nm, $R_t = 0.5$ nm, and $V_b = -11$ V. Figure 6 shows the impact of displacement on transition probability. We found that a small displacement does not affect the results by an order of magnitude compared to when the tip is directly above, i.e., $a_x = a_y = 0$. There is a small rise here at the beginning because when the tip is directly above, only the spherical harmonics corresponding to the magnetic quantum number $m = 0$ contribute, and when the tip deviates from directly above, all spherical harmonics contribute.

-
- [1] L. Kroger and C. Reich, *Nucl. Phys. A* **259**, 29 (1976).
- [2] C. W. Reich and R. G. Helmer, *Phys. Rev. Lett.* **64**, 271 (1990).
- [3] B. Seiferle, L. von der Wense, P. V. Bilous, I. Amersdorffer, C. Lemell, F. Libisch, S. Stellmer, T. Schumm, C. E. Düllmann, A. Pálffy, and P. G. Thirolf, *Nature (London)* **573**, 243 (2019).
- [4] S. Kraemer *et al.*, *Nature (London)* **617**, 706 (2023).
- [5] E. Peik and C. Tamm, *Europhys. Lett.* **61**, 181 (2003).
- [6] W. G. Rellergert, D. DeMille, R. R. Greco, M. P. Hehlen, J. R. Torgerson, and E. R. Hudson, *Phys. Rev. Lett.* **104**, 200802 (2010).
- [7] C. J. Campbell, A. G. Radnaev, A. Kuzmich, V. A. Dzuba, V. V. Flambaum, and A. Derevianko, *Phys. Rev. Lett.* **108**, 120802 (2012).
- [8] K. Beeks, T. Sikorsky, T. Schumm, J. Thielking, M. V. Okhapkin, and E. Peik, *Nat. Rev. Phys.* **3**, 238 (2021).
- [9] V. V. Flambaum, *Phys. Rev. Lett.* **97**, 092502 (2006).
- [10] J. C. Berengut, V. A. Dzuba, V. V. Flambaum, and S. G. Porsev, *Phys. Rev. Lett.* **102**, 210801 (2009).
- [11] G. A. Kazakov, A. N. Litvinov, V. I. Romanenko, L. P. Yatsenko, A. V. Romanenko, M. Schreitl, G. Winkler, and T. Schumm, *New J. Phys.* **14**, 083019 (2012).
- [12] A. D. Ludlow, M. M. Boyd, J. Ye, E. Peik, and P. O. Schmidt, *Rev. Mod. Phys.* **87**, 637 (2015).
- [13] M. Safronova, *Nature (London)* **533**, 44 (2016).
- [14] V. Barci, G. Ardisson, G. Barci-Funel, B. Weiss, O. El Samad, and R. K. Sheline, *Phys. Rev. C* **68**, 034329 (2003).
- [15] J. Thielking, M. V. Okhapkin, P. Głowacki, D. M. Meier, L. von der Wense, B. Seiferle, C. E. Düllmann, P. G. Thirolf, and E. Peik, *Nature (London)* **556**, 321 (2018).
- [16] J. Jeet, C. Schneider, S. T. Sullivan, W. G. Rellergert, S. Mirzadeh, A. Cassanho, H. P. Jossen, E. V. Tkalya, and E. R. Hudson, *Phys. Rev. Lett.* **114**, 253001 (2015).
- [17] A. Yamaguchi, M. Kolbe, H. Kaser, T. Reichel, A. Gottwald, and E. Peik, *New J. Phys.* **17**, 053053 (2015).
- [18] S. Stellmer, G. Kazakov, M. Schreitl, H. Kaser, M. Kolbe, and T. Schumm, *Phys. Rev. A* **97**, 062506 (2018).
- [19] J. Tiedau, M. V. Okhapkin, K. Zhang, J. Thielking, G. Zitzer, E. Peik, F. Schaden, T. Pronebner, I. Morawetz, L. T. De Col, F. Schneider, A. Leitner, M. Pressler, G. A. Kazakov, K. Beeks, T. Sikorsky, and T. Schumm, *Phys. Rev. Lett.* **132**, 182501 (2024).
- [20] R. Elwell, C. Schneider, J. Jeet, J. E. S. Terhune, H. W. T. Morgan, A. N. Alexandrova, H. B. T. Tan, A. Derevianko, and E. R. Hudson, [arXiv:2404.12311](https://arxiv.org/abs/2404.12311).
- [21] E. V. Tkalya, A. N. Zherikhin, and V. I. Zhudov, *Phys. Rev. C* **61**, 064308 (2000).
- [22] T. Masuda *et al.*, *Nature (London)* **573**, 238 (2019).
- [23] E. V. Tkalya, *JETP Lett.* **55**, 212 (1992).
- [24] P. V. Borisyuk, E. V. Chubunova, N. N. Kolachevsky, Y. Y. Lebedinskii, O. S. Vasiliev, and E. V. Tkalya, [arXiv:1804.00299](https://arxiv.org/abs/1804.00299).
- [25] S. G. Porsev, V. V. Flambaum, E. Peik, and C. Tamm, *Phys. Rev. Lett.* **105**, 182501 (2010).
- [26] B. S. Nickerson, M. Pimon, P. V. Bilous, J. Gugler, K. Beeks, T. Sikorsky, P. Mohn, T. Schumm, and A. Pálffy, *Phys. Rev. Lett.* **125**, 032501 (2020).
- [27] W. Wang, J. Zhou, B. Liu, and X. Wang, *Phys. Rev. Lett.* **127**, 052501 (2021).
- [28] J. Qi, H. Zhang, and X. Wang, *Phys. Rev. Lett.* **130**, 112501 (2023).
- [29] E. V. Tkalya, *Phys. Rev. Lett.* **124**, 242501 (2020).
- [30] H. Zhang, W. Wang, and X. Wang, *Phys. Rev. C* **106**, 044604 (2022).
- [31] E. V. Tkalya, *Chin. Phys. C* **45**, 094102 (2021).
- [32] S. Gargiulo, M. F. Gu, F. Carbone, and I. Madan, *Phys. Rev. Lett.* **129**, 142501 (2022).
- [33] G. Binnig, H. Rohrer, C. Gerber, and E. Weibel, *Phys. Rev. Lett.* **49**, 57 (1982).
- [34] J. Tersoff and D. R. Hamann, *Phys. Rev. Lett.* **50**, 1998 (1983).
- [35] S.-W. Hla, *J. Vac. Sci. Technol. B* **23**, 1351 (2005).
- [36] H. Oka, O. O. Brovko, M. Corbetta, V. S. Stepanyuk, D. Sander, and J. Kirschner, *Rev. Mod. Phys.* **86**, 1127 (2014).
- [37] D. M. Eigler and E. K. Schweizer, *Nature (London)* **344**, 524 (1990).
- [38] I. Shiraki, F. Tanabe, R. Hobara, T. Nagao, and S. Hasegawa, *Surf. Sci.* **493**, 633 (2001).
- [39] S. M. Hus, X.-G. Zhang, G. D. Nguyen, W. Ko, A. P. Baddorf, Y. P. Chen, and A.-P. Li, *Phys. Rev. Lett.* **119**, 137202 (2017).
- [40] C. Zhang, L. Chen, R. Zhang, and Z. Dong, *Jpn. J. Appl. Phys.* **54**, 08LA01 (2015).
- [41] R. Berndt, R. Schlittler, and J. Gimzewski, *J. Vac. Sci. Technol. B* **9**, 573 (1991).
- [42] L. von der Wense, B. Seiferle, S. Stellmer, J. Weitenberg, G. Kazakov, A. Pálffy, and P. G. Thirolf, *Phys. Rev. Lett.* **119**, 132503 (2017).
- [43] G. Dong, Y. You, and H. Dong, *New J. Phys.* **22**, 113010 (2020).
- [44] G. Dong, Z. Hu, X. Sun, and H. Dong, *J. Phys. Chem. Lett.* **12**, 10034 (2021).
- [45] J. Bardeen, *Phys. Rev. Lett.* **6**, 57 (1961).
- [46] A. D. Gottlieb and L. Wesoloski, *Nanotechnology* **17**, R57 (2006).
- [47] C. J. Chen, *Phys. Rev. B* **42**, 8841 (1990).
- [48] J. M. Eisenberg and W. Greiner, *Nuclear Theory: Excitation Mechanisms of the Nucleus* (North-Holland publishing company, North-Holland, 1976), Vol. 2.

- [49] G. Binnig and H. Rohrer, *Rev. Mod. Phys.* **59**, 615 (1987).
- [50] P. K. Hansma, V. B. Elings, O. Marti, and C. E. Bracker, *Science* **242**, 209 (1988).
- [51] Z. Lin, L. V. Zhigilei, and V. Celli, *Phys. Rev. B* **77**, 075133 (2008).
- [52] N. Minkov and A. Pálffy, *Phys. Rev. Lett.* **118**, 212501 (2017).
- [53] E. V. Tkalya, *JETP Lett.* **71**, 311 (2000).
- [54] P. Dessoic, P. Mohn, R. A. Jackson, G. Winkler, M. Schreitl, G. Kazakov, and T. Schumm, *J. Phys.: Condens. Matter* **26**, 105402 (2014).
- [55] K. Beeks, T. Sikorsky, V. Rosecker, M. Pressler, F. Schaden, D. Werban, N. Hosseini, L. Rudischer, F. Schneider, P. Berwian, J. Friedrich, D. Hainz, J. Welch, J. H. Sterba, G. Kazakov, and T. Schumm, *Sci. Rep.* **13**, 3897 (2023).
- [56] S. Stellmer, M. Schreitl, and T. Schumm, *Sci. Rep.* **5**, 15580 (2015).
- [57] X. H. Qiu, G. V. Nazin, and W. Ho, *Science* **299**, 542 (2003).
- [58] T. W. Barefoot, H. D. Ebinger, and J. T. Yates, *J. Vac. Sci. Technol. A* **15**, 2740 (1997).
- [59] J. Tersoff and D. R. Hamann, *Phys. Rev. B* **31**, 805 (1985).
- [60] Y. Zhang, Y. Luo, Y. Zhang, Y.-J. Yu, Y.-M. Kuang, L. Zhang, Q.-S. Meng, Y. Luo, J.-L. Yang, Z.-C. Dong, and J. G. Hou, *Nature (London)* **531**, 623 (2016).